



# Head-Mounting Surgical Robots for Passive Compensation of Patient Motion

Nicholas R. Posselli \*,<sup>¶</sup> Patrick S. Wellborn <sup>†,‡</sup>, Paul S. Bernstein <sup>§</sup>,  
Robert J. Webster III <sup>†</sup>, Jake J. Abbott <sup>\*</sup>

<sup>\*</sup>*Department of Mechanical Engineering and the Robotics Center  
University of Utah, Salt Lake City, UT, USA*

<sup>†</sup>*Department of Mechanical Engineering, Vanderbilt University  
Nashville, TN, USA*

<sup>‡</sup>*Titan Medical USA Inc., Chapel Hill, NC, USA*

<sup>§</sup>*Department of Ophthalmology and Visual Sciences, Moran Eye Center  
University of Utah, Salt Lake City, UT, USA*

A variety of robot-assisted surgical systems have been proposed to improve precision in the most challenging eye surgeries. However, little attention has been paid to patient motion due to breathing, snoring, talking, and other events that are common during eye surgery. This is problematic because patient motion is typically relative to a grounded surgical robot. In this paper, we characterize the benefits of a new paradigm in which robots are mounted semirigidly and noninvasively to the patient's head. This paradigm utilizes compact high-precision telerobotic systems that have been designed for this use. We present an initial design concept focused on eye surgery, and demonstrate an order-of-magnitude improvement of within-breathing-cycle motion relative to the robot compared to a pillow rest, with an optional head strap, which is the current standard of care, while essentially eliminating gross relative motion. We conduct a human-subjects study to quantify the relative motion that remains. Finally, we present an alternative design concept that leaves the patient's face unobstructed, which may be of interest for other kinds of surgery as well.

**Keywords:** Eye surgery; retinal surgery; robot-assisted surgery; microsurgery; motion compensation.

JMRR

## 1. Introduction

Many up-and-coming therapeutic protocols in ophthalmology are challenging for human surgeons to perform because they are near or beyond the limits of human motor and perceptual skills, and thus are currently attempted by only a few of the best surgeons. For

example, subretinal injection of stem cells or gene therapies requires a fine cannula to be gently placed in contact with the retina, with position subsequently held steady for up to several minutes [1] to inject a bleb of fluid. Experimental protocols to evaluate the efficacy of new therapies, which hold the promise of restoring lost vision, are confounded by the limitations in the surgeon's ability to safely and repeatably inject the therapeutic agent. Positioning accuracy as low as 10  $\mu\text{m}$  is desirable in retinal procedures due to the small structures in the retina. The retina is approximately 300  $\mu\text{m}$  thick [2], and its inner limiting membrane, capillaries, and epiretinal membrane have dimensions of approximately 3  $\mu\text{m}$  [3], 8  $\mu\text{m}$  [4], and 60  $\mu\text{m}$  [5], respectively. However, hand tremor of retinal surgeons is estimated to be substantially larger, with

Received 13 July 2023; Revised 9 September 2023; Accepted 24 December 2023; Published 19 February 2024. This paper was recommended for publication in its revised form by editorial board member, Iulian I. Lordachita.

Email address: <sup>¶</sup>[nicholas.posselli@utah.edu](mailto:nicholas.posselli@utah.edu)

NOTICE: Prior to using any material contained in this paper, the users are advised to consult with the individual paper author(s) regarding the material contained in this paper, including but not limited to, their specific design(s) and recommendation(s).

studies reporting a peak-to-peak magnitude of 108  $\mu\text{m}$  [6] and an RMS amplitude of 156  $\mu\text{m}$  [7].

Another complicating factor is head motion, which is common among patients undergoing eye surgery under monitored anesthesia (also known as conscious sedation), which makes a patient calm and drowsy but often still awake [8]. Head motion in this state is due to breathing, talking, and other voluntary and involuntary patient motions. Brogan *et al.* [9] measured the motion of 12 patients' heads during cataract surgery and found that, over the course of a procedure, head drift was 2–7 mm medially, 2–4 mm laterally, 1–5 mm superiorly, and 1–4 mm inferiorly; note that cataract surgery has substantially shorter durations ( $\sim 14$  min [10]) than retinal surgery ( $\sim 40$ – $80$  min [11]). Additionally, 16% of patients snore under monitored anesthesia, and half of those have sudden head movement during surgery [12]. Sudden movements can be unpredictable in general. Movement must be compensated by the surgeon, to the best of their ability, to avoid complications. Surgeons will often rest their hands directly on the patient's head, which serves to reduce hand tremor and couple their hands with the motion of the patient's head.

A variety of robotic systems have been proposed to improve the precision of eye surgery [13, 14], but, to date, little attention has been paid to patient head motion. In one robot-assisted *in vivo* study in humans, there was difficulty in initiating subretinal injection due to head drift [15]. Benchtop experiments with artificial or enucleated (i.e. *ex vivo*) eyes, which are typical in the development of robotic systems, rarely capture the effect of patient motion. Patient motion was simulated using a linear piezoelectric actuator that generated one-dimensional step motions in [16]. The robot in [17] could potentially simulate patient motion, as it was designed with a range of motion to accommodate patient head motion, but it was not explored. Most other benchtop setups involve a completely stationary eye, or an eye that can rotate about its center without translation. Any method of simulating patient motion will provide a more challenging evaluation of a robotic system than using a stationary eye, although generating accurate physiological motion is challenging. Limited *in vivo* studies have either placed the patient under general anesthesia [18–20] or have used a local anesthetic without conscious sedation [15, 18]. The use of general anesthesia, which results in reduced patient movement, is atypical of eye surgery and too dangerous to use as the standard of care. The use of a local anesthetic without conscious sedation is not representative of the most common cases in which anxious patients require sedation (which may affect their motion [8]).

Any clinically deployed robotic system for eye surgery will have to cope with patient motion. Active compensation (i.e. closed-loop control) can involve sensing the force between the surgical instrument and the eye [16, 21],

using visual-servoing techniques [22, 23], or moving the headrest to counteract patient movement [17]. Others have pursued passive approaches to motion compensation, which are not mutually exclusive with active approaches.

One passive approach is to immobilize the patient's head. Nasseri *et al.* [24] proposed a mechanism that would enable their manipulator to be pressed against the patient's face to form a semirigid connection, stabilizing the patient's head with respect to the robot, but the potential benefits of a such a system were not quantified. More recently, the same group proposed a mechanism that would semirigidly fix the patient's head with respect to the surgical stretcher using granular jamming [25, 26], and reported that the mechanism limited head motion to below 9 mm.

Another passive approach, motivated by mitigating motion of the eye with respect to the robot, is to form a mechanical connection between the two. One approach is to connect to the eye with suction [26, 27]. Another approach is to attach an adapter to the standard valved trocar cannulas in the sclera, which mates with a corresponding element on the robot [18]. The benefits of these approaches in terms of motion reduction have not yet been quantified. The rigidity of such connections will ultimately be limited by the compliance of the eye itself. In addition, such approaches could put the eye in danger, particularly if the patient's head is not immobilized.

Two groups (including ours) have developed compact lightweight telerobotic systems motivated by the prospect of mounting the robot directly to the patient's head to passively compensate for patient motion ([24], 306 g; [28], 800 g). This approach does not require the patient's head to be immobilized, which has hypothesized benefits in terms of patient comfort. In addition, head mounting can be combined with force sensing, visual servoing, and/or mechanical connection to the eye; head mounting will make each of these tasks easier. It is also worth noting that the robots in [24, 28], which utilize commercial piezoelectric stick-slip actuators, are also among the most precise surgical robots developed to date [13, 14]. However, neither group has actually mounted their robot on a living human, let alone quantified the benefits of head mounting. Mounting a robot to a patient's head is challenging. To rigidly mount a robot to a patient's head would require drilling into the skull, or possibly mounting to the upper jaw [29], both of which are invasive compared to current eye surgery. However, noninvasive attempts at rigid mounting are hindered by the compliance of the soft tissue surrounding the skull.

In this paper, we describe a new paradigm that enables one or more robots to be mounted semirigidly, yet noninvasively, to a patient's head. Our goal is not to immobilize the patient, but rather, immobilize the robot with respect to the patient. We first present a design concept that is

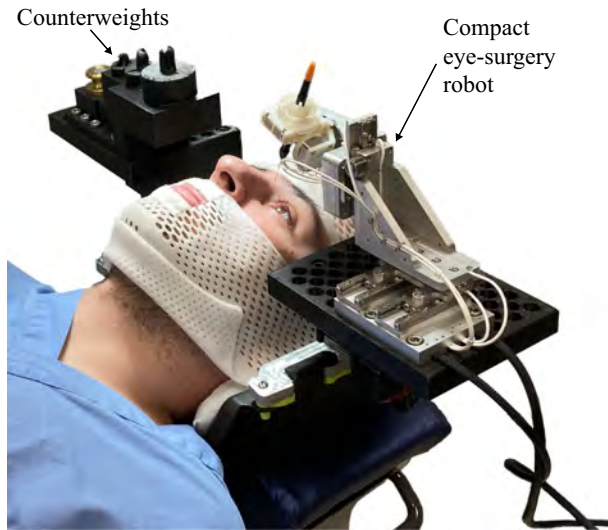


**Fig. 1.** Initial design concept for robot head-mounting. This design concept is based on a modified radiotherapy immobilization system. Since only one robot is attached (the robot described in [28]), counterweights are included on the opposite side to avoid a moment being felt by the wearer.

compatible with eye surgery (Fig. 1). We experimentally demonstrate its benefits compared to the pillow rest, with an optional head strap, which is the current standard of care; these results were originally presented in [30]. Next, we conduct a human-subjects study to characterize relative motion that can be expected between the head-mounted robot and the patient's head, due to the compliance of the soft tissue around the skull as well as the compliance in the head-mounting device itself, during gentle breathing and snoring. Finally, we present an alternative design concept that leaves the patient's face unobstructed, which may be of interest for other kinds of surgeries beyond eye surgery, such as sinus and skull-base interventions [31–33], cochlear implantation or other ear-surgery procedures [34, 35], neurosurgery [36], or any other procedure where one wishes to attach surgical instruments or tracking markers [37] rigidly, yet noninvasively, to the patient's head. We evaluate the alternative design concept experimentally and find that it performs comparably to our initial design concept, but with different logistical pros and cons. The approaches in this paper are largely agnostic to the specific robot(s) used; the results are also largely agnostic, provided the reaction forces on the robot(s), including robot-tissue interactions and inertial effects, are sufficiently small.

## 2. Initial Design Concept

Our initial design concept for noninvasively mounting one or more small robots to a patient's head is based on a modified radiotherapy immobilization system (Figs. 1–3).

Commercial radiotherapy immobilization systems based on custom-fit thermoplastic masks are used clinically to reduce relative motion between a patient's head and a linear accelerator that shoots a beam of radiation at a tumor in the patient's head. We modified a CIVCO Solstat Immobilization System (Figs. 2(a)–2(c)) to enable one or more surgical robots to be mounted semirigidly to a patient's head. The Solstat includes a bowl with a flat posterior surface (Fig. 2(a)). A CIVCO AccuForm cushion, which hardens to retain its shape when exposed to water, is placed inside of the bowl and is formed to the shape of the patient's head (Fig. 2(b)). A CIVCO custom-fit thermoplastic mask is formed to the shape of the patient's face, and is then attached to the bowl using quick-release latches (Fig. 2(c)). The Solstat's masks are already compatible with standard surgical draping during eye surgery, as well as oxygen supply via the nose. We removed the component that is used to rigidly attach the Solstat to a table during radiotherapy, making it compatible with standard stretcher pillows.

To increase the stiffness of the Solstat and provide features for mounting one or more robots, we created an 8-mm-thick U-shaped aluminum mounting plate that fits over the rim of the thermoplastic mask (Fig. 2(d)). Screws are inserted in the plate, which self-tap into holes in the rim of the thermoplastic mask. Modified versions of the Solstat's quick-release latches attach the mask to the bowl while accommodating the additional thickness of the aluminum plate (Fig. 2(e)). On/off magnets (Industrial Magnetics flanged magnetic jig JF095R) are connected to the left and right sides of the mounting plate, enabling ferromagnetic robot-mounting hardware to be connected to the mounting plate after surgical draping has already been placed over the plate (Fig. 2(f)); the mounting hardware could easily be changed to accommodate multiple robots per magnet so that a robot could be mounted in a superior position if desired. Plastic guides facilitate the correct placement of ferromagnetic mounting hardware. A steel plate, which magnetically attaches to the on/off magnet, is used to mount a robot to the aluminum mounting plate. A variety of compact robots could be mounted, provided that appropriate mounting hardware is used to connect the robot to the steel plate and place the robot in a desired position. In the case of the robot described in [28], we use the 3D-printed plastic breadboard component shown in Fig. 2(g) to enable gross repositioning.

Figure 3 shows how the initial design concept can be used to mount robots and counterweights to a patient's head without modifying standard surgical draping. A potential workflow is as follows:

1. Before surgery, the custom-fit cushion and mask are formed. This could be done before the day of surgery.
2. During the same visit, the position of the patient's eye is measured relative to the steel mounting plate so that



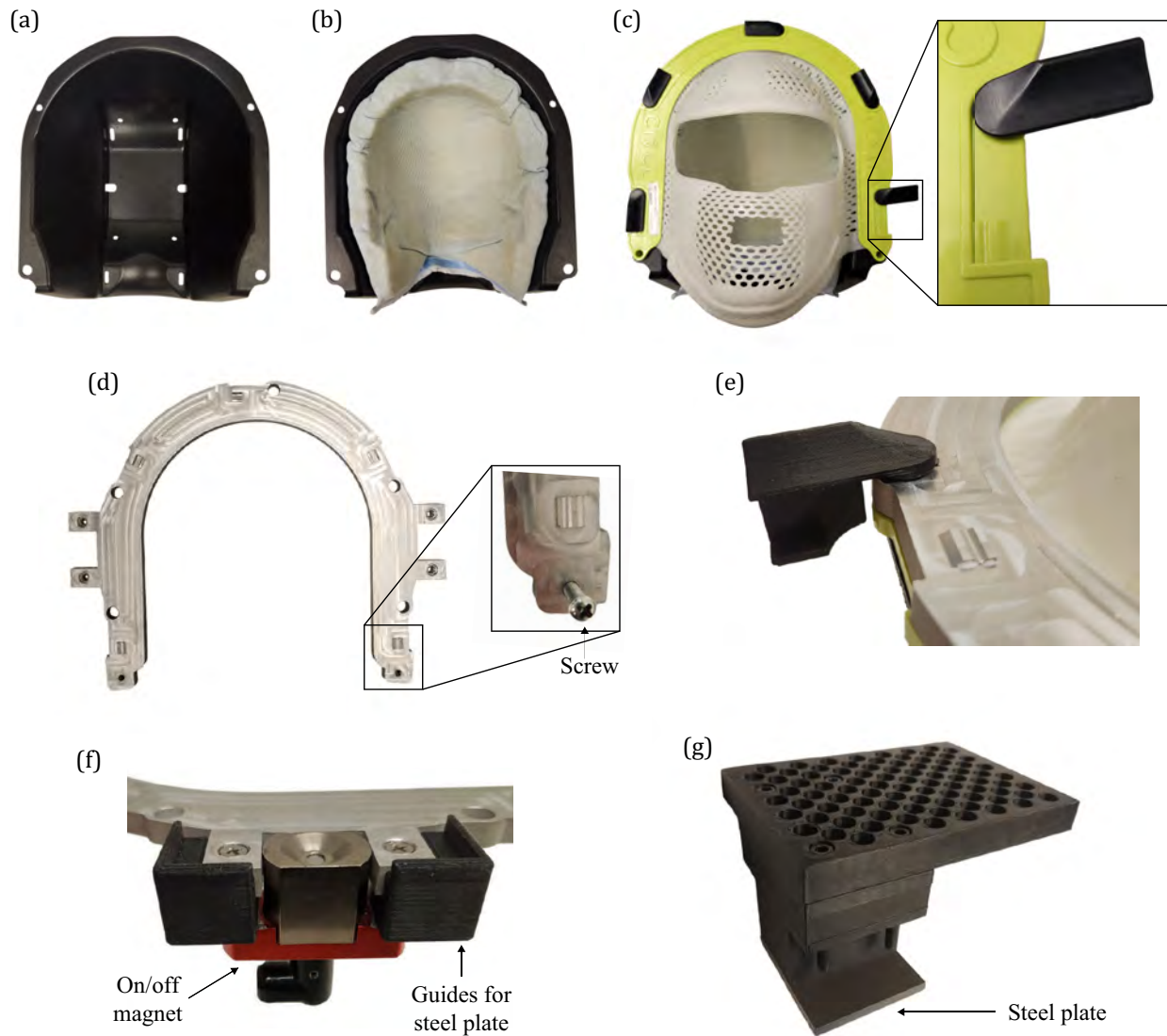


**Fig. 2.** Design features of our initial design concept. (a) CIVCO Solstat bowl. (b) Custom-fit CIVCO AccuForm cushion. (c) CIVCO custom-fit thermoplastic mask attached to bowl using quick-release latches. (d) Aluminum mounting plate. (e) Modified quick-release latch. (f) On/off magnet and alignment guides for steel plate. (g) Steel plate with hardware for robot placement.

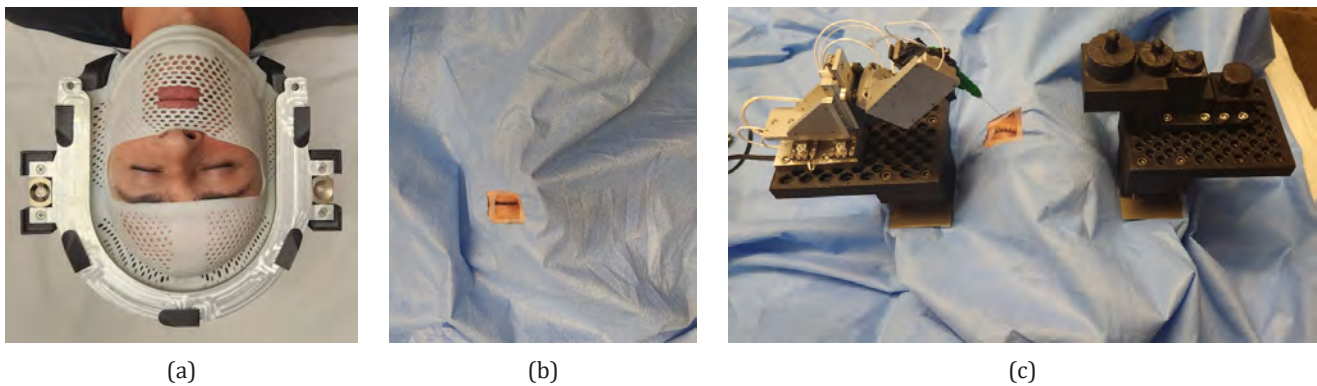


**Fig. 3.** Use of our initial design concept with standard, unmodified, surgical draping, shown from the surgeon's perspective. (a) The aluminum mounting plate is used to attach the thermoplastic mask. (b) Standard surgical draping is placed over the mask. (c) Robots and counterweights are magnetically connected to the mounting plate, using on/off magnets, through the draping.

the robot can be optimally attached to the robot-place-ment hardware (Fig. 2(g)).

3. During surgery, the thermoplastic mask and aluminum mounting plate are placed on the patient's face and attached to the Solstat bowl (Fig. 3(a)).
4. The region around the patient's eye is sterilized.
5. Surgical draping is applied over the patient's face (Fig. 3(b)), using the same draping process used in manual surgery.
6. Trocar cannulas are inserted into the eye in the standard positions.
7. Any other preliminary surgical tasks that do not require the use of the robot are performed.
8. Using the steel plate (Fig. 2(g)), and the magnet under the draping, one or more robots are magnetically connected through the draping (Fig. 3(c)). The robot(s) would likely be within their own sterile bags.

The weight of the robot(s) is not felt by the wearer's face or neck; it is distributed to the pillow by the structure of the head-mounting device. It is worth noting that, in the event of an emergency, the robot and its attached steel plate can be torqued off of the on/off magnet without using the on/off magnet's handle (which is under the draping), and the mounting plate and thermoplastic mask can be unlatched and removed in approximately 5 s.

### 3. Demonstration of the Relative Benefit of Head Mounting

In this section, we perform a study to evaluate the benefit of head mounting compared to two control conditions that represent cases where a surgical robot would be mounted to the surgical stretcher or an adjacent table. Specifically, we quantify movement of the eye orbit relative to a static world frame in three conditions—the head resting on the pillow (C1), the head strapped down to the pillow (C2), and the head when wearing our head-mounting prototype on the pillow (C3)—and in this final condition, to quantify the movement of the head-mounted robot relative to the eye orbit (C4). C1 and C2 (Figs. 4(a) and 4(b)) are control conditions that represent cases where a surgical robot would be mounted to the surgical stretcher or an adjacent table. In C3 and C4, since we only used one robot (which is a modification of the robot described in [28]), counterweights were attached to the head mount to eliminate an applied moment (Fig. 4(c)).

The participant (who is an author) lay supine on a Hillrom eye-surgery stretcher, and the positions of colored markers were tracked by a Sony PMW-10MD camera recording video through the lens of a Leica ophthalmic microscope, using one colored marker attached to swim goggles that are effectively rigidly connected to the eye orbits (Fig. 4(c)), and one colored marker attached to the end-effector of the robot (when the robot

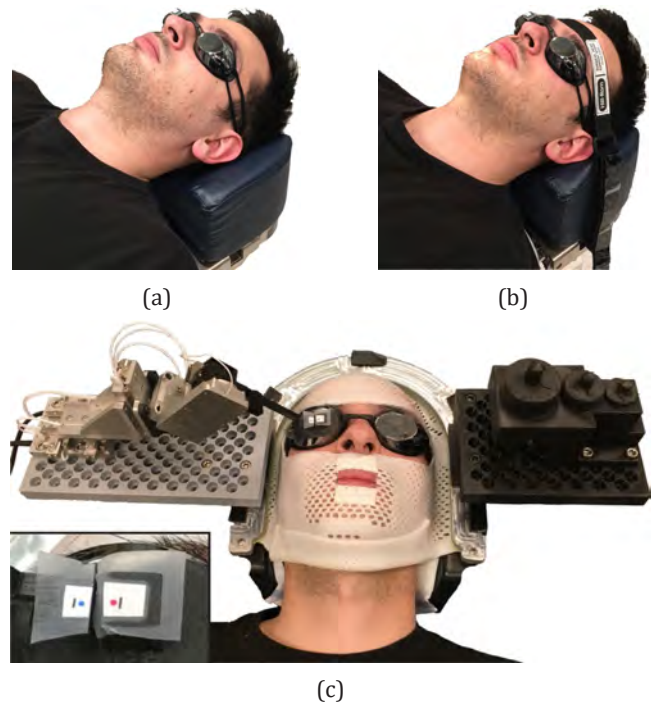


**Fig. 4.** Experimental setup for the study comparing head mounting with control conditions. (a) Head resting on pillow (condition C1). (b) Strap holding head tightly on pillow (condition C2). (c) System shown fitted with one robot (on left) and counterweights for balance (on right). The inset shows a zoomed view of the tracking markers placed on the end-effector of the robot (blue dot, on left) and on the goggles (red dot, on right) that are used to quantify the displacement of the robot relative to the goggles (condition C4), as well as the goggles themselves (condition C3) due to motion of the wearer. The black scale bars next to the tracking markers are 2.0 mm long.

was present). The markers were localized in the images during post-processing. Color thresholding was used to isolate the pixels belonging to the colored circles on the tracking markers in each video frame. The isolated pixels were used to calculate each circle's centroid in each video frame. Scale bars with lengths of 2.0 mm on the markers (see Inset of Fig. 4(c)) were used to determine the conversion from pixels to millimeters.

The participant mimicked two actions that commonly occur during eye surgery: gentle (but not shallow) breathing and deep snoring-like rapid inhalations. For each action, independent videos were recorded for each inhale-exhale cycle, each starting fully exhaled and ending fully exhaled.

We indicate the position of the colored marker on the goggles using the vector  ${}^c d_{cg}$ , where the two symbols in the right subscript indicate that the vector goes from the origin of the microscope-camera frame  $c$  to the colored marker on the goggles (i.e. the origin of goggle frame  $g$ ), and the left superscript indicates the vector is represented in microscope-camera frame  $c$ . Analogously, we indicate the position of the colored marker on the robot

as  ${}^c\mathbf{d}_{cr}$ , from which we can calculate the position of the goggles with respect to the robot as

$${}^c\mathbf{d}_{rg} = {}^c\mathbf{d}_{cg} - {}^c\mathbf{d}_{cr}. \quad (1)$$

We quantify the relative displacement of the goggles with respect to a given frame  $i$ , at each instant, as.

$$\delta(t) = \|{}^c\mathbf{d}_{ig}(t) - {}^c\mathbf{d}_{ig}(t_0)\|, \quad (2)$$

where  $\delta(t)$  is calculated separately for each video segment (i.e. breathing cycle) and  ${}^c\mathbf{d}_{ig}(t_0)$  is the relative position in the first frame of the corresponding video segment,  $i = c$  indicates the origin of the microscope-camera frame for conditions C1–C3, and  $i = r$  indicates the origin of the robot frame for condition C4. To quantify the amount of motion between frame  $i$  and the goggles, we calculate the maximum displacement for each video segment (i.e. breathing cycle) as

$$\delta_{\max} = \max_{\text{seg}}(\delta(t)). \quad (3)$$

Typical examples of the relative displacements observed in condition C4, for gentle breathing and snoring-like rapid inhalations, are provided in Fig. 5. During snoring-like movements, relative motion is principally in the sagittal plane, as expected. During gentle breathing, relative motions are smaller and their principal directions are less pronounced.

Figure 6 shows maximum within-breathing-cycle displacement of the goggles relative to the static camera frame (and thus of the eye orbit relative to a hypothetical stretcher/table mounted robot) was as high as 2.2 mm for gentle breathing and 5.2 mm during snoring-like movements with the control conditions. Although the

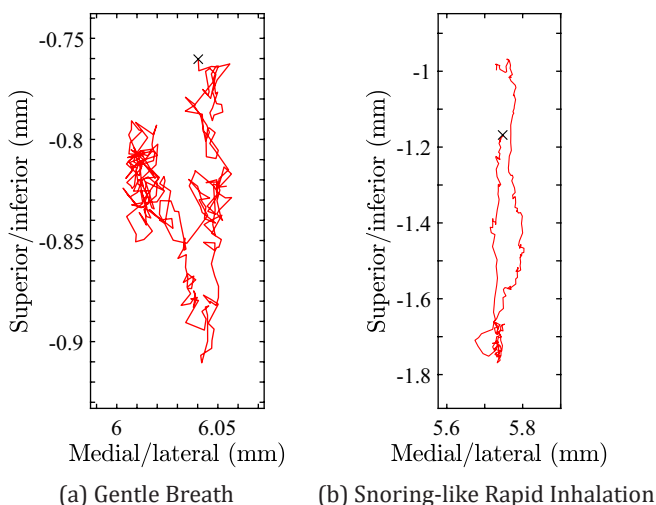


**Fig. 5.** Typical trajectories of  ${}^c\mathbf{d}_{rg}(t)$  for condition C4, for a single gentle breath and a single snoring-like rapid inhalation. The initial condition  ${}^c\mathbf{d}_{rg}(t_0)$  is denoted by  $\times$ . Note the difference in axis scaling.

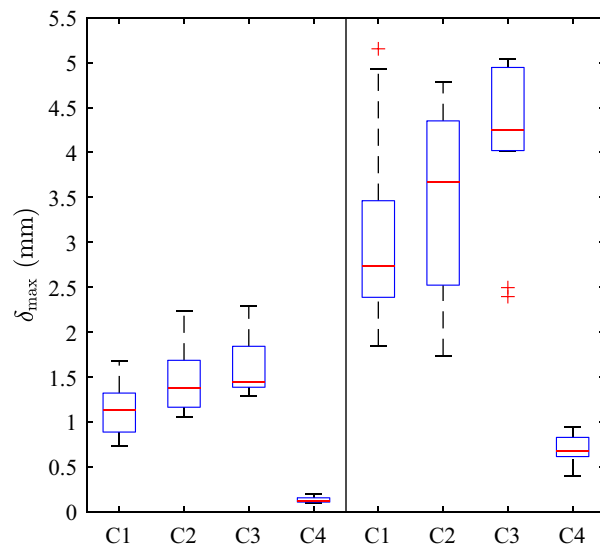


**Fig. 6.** Box-whisker plots ( $n = 11$ ) of the maximum displacement within a given breathing cycle of the goggles with the head resting on the pillow (C1), the head strapped to the pillow (C2), and the head when wearing the head-mounting system (C3), as well as maximum displacement of the head-mounted robot relative to the goggles (C4), for gentle breathing (left) and snoring-like rapid inhalations (right).

head strap may be effective at reducing gross motions of the head, it was ineffective at mitigating these relatively small within-breathing-cycle motions. The largest movement of our head-mounted robot relative to the goggles (and thus to the eye orbit) was 0.2 mm for gentle breathing and 0.9 mm for snoring-like movements. Analysis of variance, using a Bonferroni correction for multiple comparisons, indicates that these differences are significant ( $p < 0.001$ ) for both types of movement for this wearer. Note that our head-mounting device did not reduce head motion, and may have even slightly increased it (although not significantly); the observed benefit of head-mounting does not stem from reducing absolute head motion.

#### 4. Human-subjects Study Quantifying Maximum Relative Displacement

In this section, we conduct a human-subjects study to quantify the distribution of maximum displacements of the robot relative to the eye orbit that we can expect from head mounting, using a broader sample of participants. We do not revisit the control conditions.

Our study comprised four adult males and four adult females, under the approval of the University of Utah Institutional Review Board. All research was performed in accordance with relevant guidelines and regulations. Written informed consent was obtained from all individuals. Participant information is provided in Table 1. Participant 8, who is one of the authors of this paper, was



**Table 1.** Participant information and experimental settings. Circumference of the head is in units cm, Resolution of the camera is in units  $\mu\text{m}/\text{pixel}$ , F = female, M = male, L = long hair, S = short hair, B = bald, GB = gentle breathing, SN = snoring-like rapid inhalations.

Participant	1	2	3	4	5	6	7	8
Sex	F	M	M	F	F	M	F	M
Age (years)	29	30	20	25	23	28	50	45
Circumference	54	57	58	58	56	57	57	58
Hair	L	S	S	L	L	S	L	B
Resolution, GB	7	8	9	8	6	8	9	6
Resolution, SN	12	11	12	12	9	11	14	11

included because we wanted to include a participant with a smooth bald head.

The experiment was identical to the one described in Sec. 3, except we only considered the movement of the head-mounted robot relative to the goggles (i.e. C4). The zoom level of the microscope was kept constant for all of a participant's breathing cycles for each breathing type, and was adjusted when changing to a different participant or breathing type in an attempt to maximize resolution while ensuring that the markers never left the frame. The tracking resolutions provided in Table 1 were approximated by dividing the physical lengths of the scale bars (i.e. 2000  $\mu\text{m}$ ) by their lengths in the video frames (in pixels). Before the first video recording, the robot end-effector was positioned such that the marker on the robot end-effector was next to the marker on the goggles, at which point the robot was not moved again; the robot's joints are effectively rigid when no force is applied due to their stick-slip nature, but no assumption of rigidity is required since we are tracking the end-effector.

Like in Sec. 3, we measured within-breathing-cycle maximum displacements,  $\delta_{\text{max}}$ , relative to the beginning of each video segment. For this experiment, we also consider displacements relative to the beginning of the first video segment for each participant and action to account for drift across breathing cycles:

$$\Delta(t) = \|\mathbf{d}_{ig}(t) - \mathbf{d}_{ig}(0)\|, \quad (4)$$

where  $\mathbf{d}_{ig}(0)$  is the relative position in the first frame of the first video segment for a given participant and breathing type. We then calculate the largest value of  $\Delta(t)$  that occurs within each video segment, which we denote as

$$\Delta_{\text{max}} = \max_{\text{seg}}(\Delta(t)), \quad (5)$$

for that video segment. A surgeon controlling a head-mounted robot can likely compensate for a slow drift between a head-mounted robot and a patient's eye that occurs over the course of several breathing cycles (captured by  $\Delta_{\text{max}}$ ), as they do in traditional surgery,

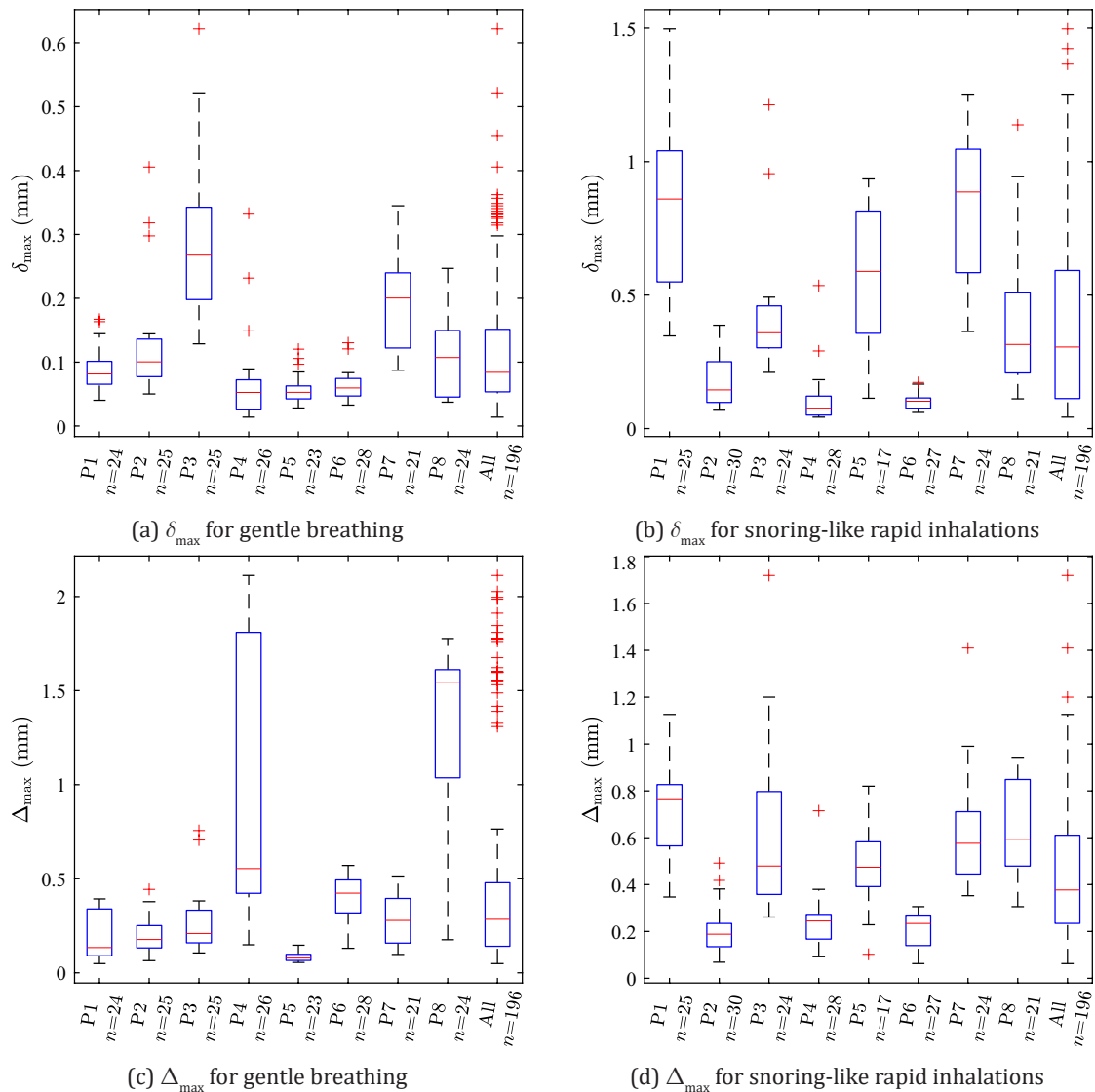
whereas shifts that take place over shorter time scales (captured by  $\delta_{\text{max}}$ ) are more difficult for a surgeon to actively compensate.

Figure 7 shows maximum displacements,  $\delta_{\text{max}}$  and  $\Delta_{\text{max}}$ , that occurred during gentle breathing and snoring-like rapid inhalations for each participant. In each plot, the rightmost box-whisker includes the combined data from all participants. The maximum within-breathing-cycle displacements for gentle breathing,  $\delta_{\text{max}}$ , across all participants were as high as 0.62 mm, but displacements above 0.3 mm were relatively uncommon (see Fig. 7(a)). The displacements over the course of all gentle-breathing cycles,  $\Delta_{\text{max}}$ , were under 1 mm for most participants (see Fig. 7(c)); however,  $\Delta_{\text{max}}$  for participants P4 and P8 were as high as 2.11 mm and 1.78 mm, respectively (see Discussion). For snoring-like rapid inhalations,  $\delta_{\text{max}}$  was as high as 1.50 mm, but typically did not exceed 1.25 mm (see Fig. 7(b));  $\Delta_{\text{max}}$  was as high as 1.72 mm, but typically did not exceed 1.13 mm (see Fig. 7(d)).

## 5. Estimating 3D Displacements from High-resolution 2D Measurements

In Secs. 3 and 4, we showed results from studies where a high-resolution microscope camera (Table 1 indicates a tracking resolution of  $<15 \mu\text{m}$ ) was used to measure displacements in the horizontal plane. In this section, we use 3D-displacement data from a lower-resolution optical tracker to estimate 3D displacements from the microscope camera's high-resolution 2D displacements.

Two of the authors were the participants for the collection of 3D-displacement data. Each participant lay on a Hillrom eye-surgery stretcher, with the initial design concept placed on a flat sheet of plastic (Fig. 8). The motions of the participant's skull and the head-mounting prototype were measured using a Northern Digital Polaris Spectra optical tracker, which has a reported 3D RMS repeatability of  $\leq 150 \mu\text{m}$ . The position of the participant's skull, by way of the upper jaw, was measured using a rigid body comprising four retro-reflective navigation markers, which was mounted on a modified CIVCO Precise Bite mouthpiece that was custom-fit to the participant. The position of the head-mounted robot was measured using another four-marker rigid body, which was attached to a component on the head-mounting device that served as a stand-in for the robot. The optical tracker was placed such that one of its coordinate axes was vertical. The tracker was superior to the participant such that both sets of retro-reflective markers were detected by the tracker. A set of masses totalling 800 g was used to simulate the weight of the robot described in [28]. Because the masses representing the weight of the robot were placed on one side of the head, counterweights on the other side were used to eliminate an applied moment that would need to be supported by the participant's neck.



**Fig 7.** Box-whisker plots of relative motion for participants 1–8 as well as for the combined data of all participants, quantified by the maximum displacements (a)  $\delta_{\max}$  for gentle breathing, (b)  $\delta_{\max}$  for snoring-like rapid inhalations, (c)  $\Delta_{\max}$  for gentle breathing, and (d)  $\Delta_{\max}$  for snoring-like rapid inhalations. Note the difference in axis scaling.

Participants again mimicked gentle breathing and snoring. For the case of gentle breathing, the participants took gentle breaths, and motion was recorded for 70 s. For the case of snoring, a “beep” sound was played every 3 s for a total of 21 s (i.e. seven cycles), and the participants, following each beep, inhaled sharply and then exhaled. We eliminated the first 10 s of data for each set of gentle-breathing data to ensure that the participants were settled into a comfortable breathing cycle, leaving 60 s for analysis. For the snoring data, we eliminated the first 3 s (i.e. the first inhale-exhale cycle) to ensure that the participants were settled into a comfortable cycle, leaving 18 s for analysis.

The data obtained by the optical tracker was recorded at a rate of 60 Hz and contained the pose (i.e. position and orientation) of each four-marker rigid body. Each

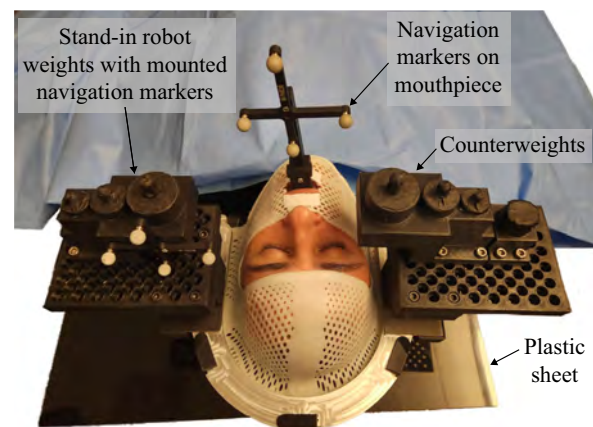


**Fig. 8.** Experimental setup used to record 3D relative displacements for the initial design concept.



pose was measured in the coordinate frame of the optical tracker, which we denote frame  $o$ . We indicate the position of the four-marker rigid body mounted to the bite piece using the vector  ${}^o\mathbf{d}_{ob}$ , where the two symbols in the right subscript indicate that the vector goes from the origin of frame  $o$  to the origin of the bite-piece frame  $b$ , and the left superscript indicates the vector is represented in the optical tracker frame  $o$ . Similarly, we indicate the vector representing the position of the four-marker rigid body mounted to the head-mounting prototype as  ${}^o\mathbf{d}_{oh}$ . We represent the orientation of the bite-piece (i.e. skull) frame and head-mounting prototype frame using the rotation matrices  ${}^oR_b$  and  ${}^oR_h$ , respectively.

We took the Fourier transform of the z-component of  ${}^o\mathbf{d}_{ob}$  (which captures superior/inferior movement of the bite piece) for the gentle breathing results in order to measure the breathing frequency of each participant. We found that Participants 1 and 2 breathed with frequencies of 0.086 Hz and 0.314 Hz, respectively, which correspond to periods of 11.6 s and 3.2 s, respectively. The 60 s gentle-breathing sets of data were then segmented into five 11.6 s segments and 18 3.2 s segments, respectively. Because the frequency of snoring was dictated by the 3-s intervals between beeps, we manually segmented each set of snoring data into six segments.

In Secs. 3 and 4, the tracking marker representing the position of the eye was attached to a goggles lens and had a coordinate frame  $g$  (Fig. 4(c)). To account for the discrepancy between the position of the tracking markers on the bite piece used in this section and the position of the goggles-mounted marker used previously, we took preliminary measurements in which each participant wore the bite piece (with frame  $b$ ) and goggles approximating the position of the eye (with frame  $g$ ), each with tracking markers attached. We calculated the fixed rigid-body transformation between them as

$${}^b\mathbf{d}_{bg} = {}^oR_b^T ({}^o\mathbf{d}_{og} - {}^o\mathbf{d}_{ob}). \quad (6)$$

Similarly, in Secs. 3 and 4, the tracking marker representing the tip of the surgical instrument was attached to the end-effector of the robot and adjusted such that it was in close proximity to the goggles-mounted tracking marker (Fig. 4(c)). To account for the discrepancy between the position of the tracking markers on the head-mounted stand-in robot used in this section (with frame  $h$ ) and the position of the end-effector-mounted marker (with frame  $r$ ) in previous experiments, we calculated a constant rigid-body transformation between them as follows. For each set of breathing data, we take the initial measurement (i.e. at time  $t = 0$ ) of  ${}^oR_h$ ,  ${}^oR_b$ ,  ${}^o\mathbf{d}_{oh}$ , and  ${}^o\mathbf{d}_{ob}$  and calculate the fixed rigid-body transformation from frame  $r$  to frame  $h$  as

$${}^h\mathbf{d}_{rh} = {}^oR_h^T ({}^o\mathbf{d}_{oh} - {}^o\mathbf{d}_{or}), \quad (7)$$

where  ${}^o\mathbf{d}_{or}$  is calculated using the initial position of frame  $g$  as an approximation for the initial position of frame  $r$  (because the markers for frames  $g$  and  $r$  were placed in close proximity to each other in previous experiments):

$${}^o\mathbf{d}_{or} \approx {}^o\mathbf{d}_{og} = {}^o\mathbf{d}_{ob} + {}^oR_b^b\mathbf{d}_{bg}. \quad (8)$$

We then represent the position of frame  $g$  (i.e. the eye) relative to frame  $r$  (i.e. the tip of a robot-mounted instrument) as

$${}^o\mathbf{d}_{rg} = {}^oR_h^h\mathbf{d}_{rh} + {}^o\mathbf{d}_{hb} + {}^oR_b^b\mathbf{d}_{bg}, \quad (9)$$

where  ${}^o\mathbf{d}_{hb} = {}^o\mathbf{d}_{ob} - {}^o\mathbf{d}_{oh}$ , and where the quantities  ${}^oR_h$ ,  ${}^oR_b$ ,  ${}^o\mathbf{d}_{oh}$ , and  ${}^o\mathbf{d}_{ob}$  are time-varying in general.

We quantify the total (i.e. 3D) displacements between the eye and the robot-mounted instrument, at each instant, by first calculating the mean relative position over the entire data set:

$$\overline{{}^o\mathbf{d}_{rg}} = \frac{1}{N_{\text{tot}}} \sum {}^o\mathbf{d}_{rg}(t), \quad (10)$$

and then calculating the distance from the mean at each instant

$$\Delta_T(t) = \| {}^o\mathbf{d}_{rg}(t) - \overline{{}^o\mathbf{d}_{rg}} \|. \quad (11)$$

The horizontal displacements,  $\Delta_H(t)$ , are calculated similarly, but using only the horizontal components of  ${}^o\mathbf{d}_{rg}(t)$  (i.e. the projection of  ${}^o\mathbf{d}_{rg}(t)$  onto the 2D horizontal plane). The vertical displacements,  $\Delta_V(t)$  are calculated using only the vertical components of  ${}^o\mathbf{d}_{rg}(t)$  (i.e. the projection of  ${}^o\mathbf{d}_{rg}(t)$  onto the 1D vertical line). Finally, the maximum displacements over each data segment (i.e. breathing cycle) are calculated as

$$\Delta_{T,\text{max}} = \max_{\text{seg}}(\Delta_T(t)), \quad (12)$$

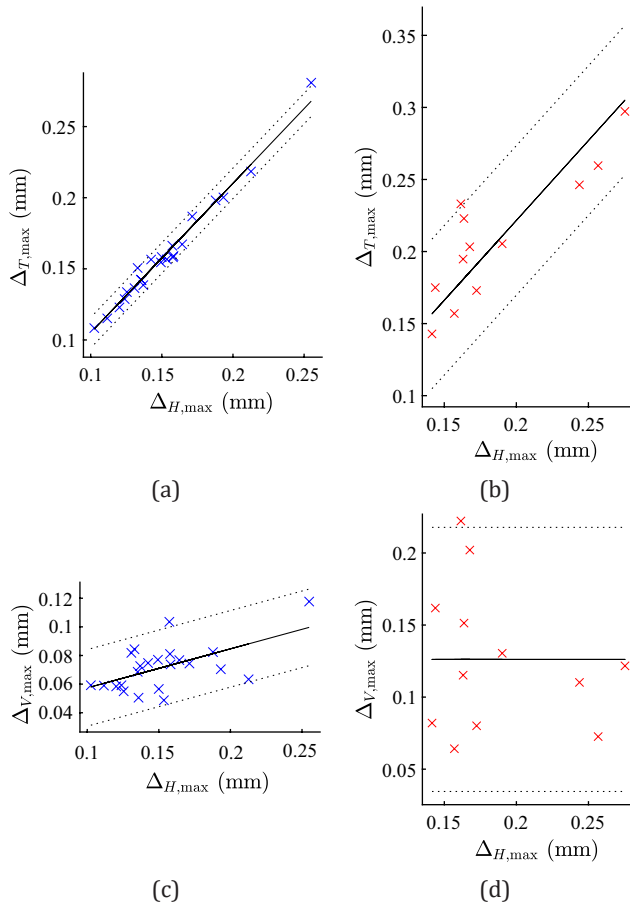
$$\Delta_{H,\text{max}} = \max_{\text{seg}}(\Delta_H(t)), \quad (13)$$

$$\Delta_{V,\text{max}} = \max_{\text{seg}}(\Delta_V(t)). \quad (14)$$

We perform linear regression to estimate intercepts and slopes in the relationships between  $\Delta_{H,\text{max}}$  and  $\Delta_{T,\text{max}}$  and between  $\Delta_{H,\text{max}}$  and  $\Delta_{V,\text{max}}$  for both gentle breathing and snoring-like rapid inhalations. For each relationship, if a parameter (i.e. slope or intercept) is not significantly different from zero (using a standard significance of  $\alpha = 0.05$ ), then we repeat the regression without that parameter until we obtain a parsimonious model. Table 2 contains the regression results, which include the 95% confidence intervals on the original regression parameters prior to eliminating terms, the parsimonious-model parameters, and the standard deviations of the residual

**Table 2.** Parsimonious-model parameters and regression statistics for  $\Delta_{T,\max} = \alpha \Delta_{H,\max} + \beta$  and  $\Delta_{V,\max} = \alpha \Delta_{H,\max} + \beta$  for gentle breathing (GB) and snoring-like rapid inhalations (SN).

Relationship	$\Delta_{T,\max}$ vs. $\Delta_{H,\max}$		$\Delta_{V,\max}$ vs. $\Delta_{H,\max}$	
	GB	SN	GB	SN
Breathing type	GB	SN	GB	SN
95% CI on original $\alpha$	[1.02, 1.15]	[0.49, 1.20]	[0.10, 0.45]	[-1.02, 0.48]
95% CI on original $\beta$ ( $\mu\text{m}$ )	[-16, 5]	[-15, 119]	[3, 58]	[33, 321]
Parsimonious $\alpha$	1.05	1.11	0.27	0
Parsimonious $\beta$ ( $\mu\text{m}$ )	0	0	30	126
Standard deviation of residuals ( $\mu\text{m}$ )	5	26	13	46

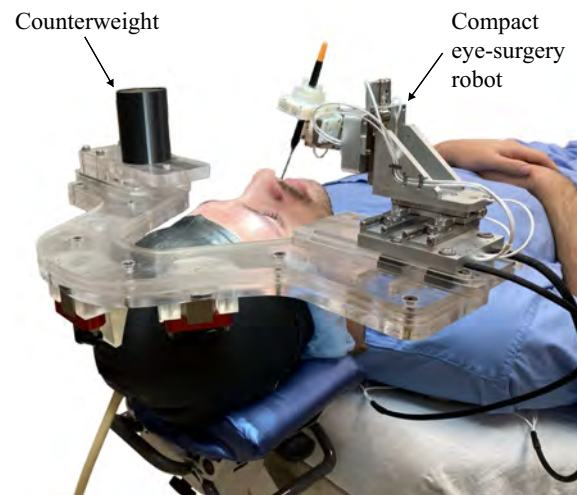
**Fig. 9.** Parsimonious model (solid line) with  $\pm 2$  standard deviations of the model residuals (dotted lines) for relationship between maximum horizontal displacements  $\Delta_{H,\max}$  and (a) maximum total (i.e. 3D) displacements  $\Delta_{T,\max}$  for gentle breathing, (b)  $\Delta_{T,\max}$  for snoring-like rapid inhalations, (c) maximum vertical displacements  $\Delta_{V,\max}$  for gentle breathing, and (d)  $\Delta_{V,\max}$  for snoring-like rapid inhalations.

error of the parsimonious model. Figure 9 shows the parsimonious models with bounds showing  $\pm 2$  standard deviations of the model residuals. The model relating maximum horizontal displacements to total displacements for gentle breathing has relatively high predictive power, and indicates that total (i.e. 3D) displacements can be estimated by multiplying the horizontal-displacement

measurements from gentle breathing by 1.05. Similarly, total displacements from snoring and vertical displacements from gentle breathing can be estimated from the parsimonious-model parameters, although the predictive power is somewhat lower (as indicated by the standard deviations of the residuals). Finally, vertical displacements for snoring-like rapid inhalations are not correlated with the horizontal displacements that are measured; the maximum vertical displacement should be estimated as  $126 \pm 92 \mu\text{m}$  regardless of the magnitudes of horizontal displacements.

## 6. Alternative Design Concept

We designed an alternative concept that leaves the face of the patient unobstructed (Figs. 10, 11, and 12). It is based on granular jamming, particularly the granular-jamming cap described in [37] that semirigidly fixed retro-reflective fiducial markers to a patient's head to improve

**Fig. 10.** Alternative design concept for robot head-mounting. The concept is based on a granular-jamming cap. Since only one robot is attached (the robot described in [28]), counterweights are included on the opposite side to avoid a moment being felt by the wearer.

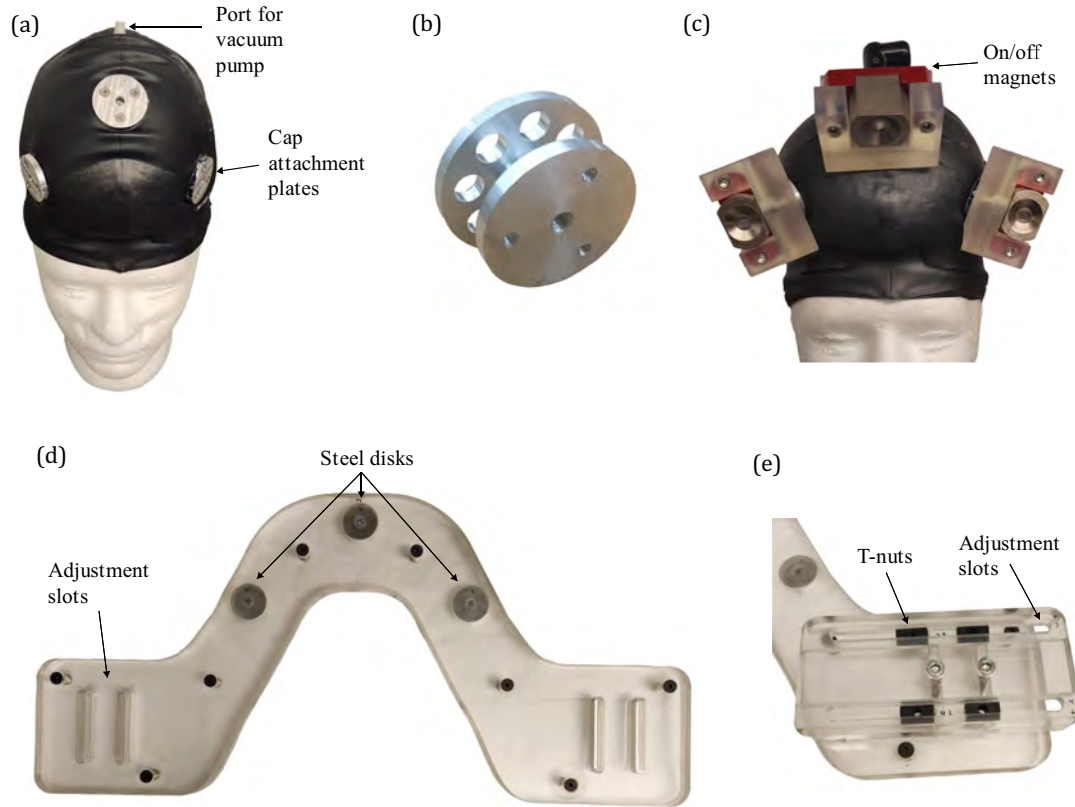


**Fig. 11.** Design features of our alternative design concept. (a) Granular-jamming cap, which includes plastic granules enclosed by two nested caps that are glued together. A port at the top of the outer cap enables air to be removed from the space between the outer and inner caps using a vacuum pump, which causes the granules to jam together, making the cap rigid. Cap attachment plates enable robot-mounting hardware to be fastened to the cap. (b) Three aluminum anchors, which are embedded inside of the cap and become fixed in place inside of the cap when air is removed, enable the attachment of the cap attachment plates. (c) On/off magnets attach to the cap via the embedded anchors. (d) Acrylic mounting plate with attached steel disks for magnetically connecting to the on/off magnets and slots for adjustable positioning of attached robots. (e) Sliding robot-attachment plate with T-nuts for attaching robots/counterweights and slots for further robot-position adjustment.

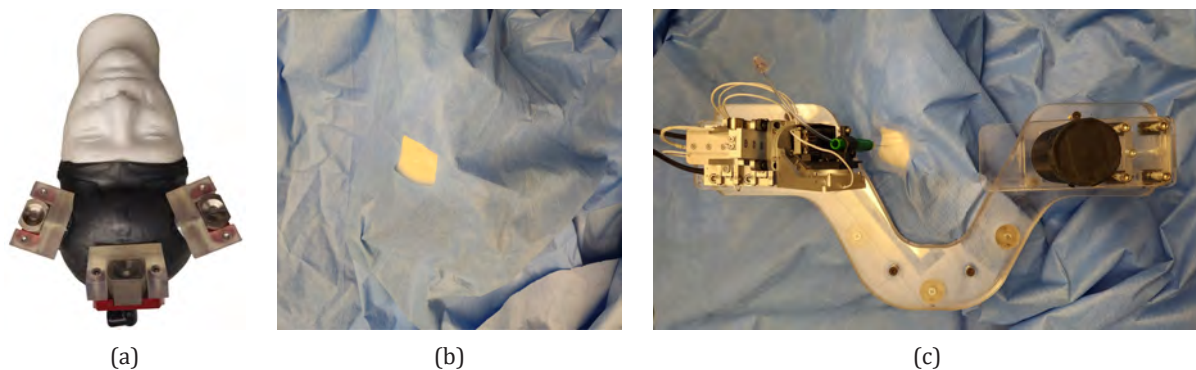


**Fig. 12.** Use of our alternative design concept with standard, unmodified, surgical draping, shown from the surgeon's perspective. (a) On/off magnets attached to the soft granular-jamming cap. (b) Standard surgical draping is placed over the cap and magnets. (c) The acrylic mounting plate, with attached robots and counterweights, is magnetically connected to the on/off magnets through the draping. A vacuum pump is then used to remove the air from the cap to make it rigid.

accuracy in image-guided surgical procedures involving the head. We extended the concept of [37] to enable one or more surgical robots to be mounted to a patient's head (Fig. 11). Similar to the cap in [37], ours consists of two

silicone caps, with one smaller one nested within a larger one. A granular material, a plastic grit soft abrasive blasting medium with a particle size of 0.595–0.841 mm (mesh size 20–30, McMaster-Carr, Elmhurst, IL) fills the space



between the two caps before they are sealed in an airtight fashion to one another around the brim of the caps using silicone adhesive (Fig. 11(a)). A port is embedded in the cap, which enables connection of a vacuum pump.

Upon placing the cap on the patient's head, it conforms to the contours of the skull. Most notably, it fills in the natural concavity at the patient's temple between the sphenoid and temporal bone, as well as wraps around the skull. Once in place, a vacuum is drawn via the port on the outer cap, which compresses the granules, and the device solidifies as the granules jam together. Three round aluminum anchors (Fig. 11(b)) are embedded in the cap and surrounded by the granules. When the air is removed, they are fixed in place relative to the cap. Three round aluminum plates on the exterior of the cap attach to the anchors using screws that pierce the outer cap. Although the screws pierce the outer cap, there is an airtight seal resulting from the anchors and plates tightly sandwiching the outer cap. A threaded hole in the center of the anchor enables robot-mounting hardware to be attached to the cap through a hole in the outer cap. For the purpose of maintaining an airtight seal, the hole does not extend through the entire length of the anchor, and the hole in the cap is sealed by sandwiching the surrounding outer cap material between the anchor and the external plate.

Stereolithography-printed components fastened to the center holes in the anchors are used to mount on/off magnets (Fig. 11(c)). An acrylic mounting plate (Fig. 11(d)) magnetically connects to the on/off magnets using three steel disks that are attached to the plate. The plate contains slots on the left and right sides, which enable the positions of attached hardware to be adjusted superiorly/inferiorly relative to the patient. Additional robot attachment plates are bolted to the main mounting plate (Fig. 11(e)) and contain slots that enable attached hardware to be adjusted medially/laterally relative to the patient. T-nuts that slide in the slots are used to attach robots and counterweights.

Figure 12 shows how this design concept can be used to mount robots and counterweights to a patient's head without modifying standard surgical draping. A potential workflow is as follows:

1. The cap is placed on the patient's head, and the stereolithography-printed magnet holders are attached to the anchors. The on/off magnets are then attached to the magnet holders (Fig. 12(a)). A nonsterile alignment fixture that mimics the acrylic mounting plate is then attached to the on/off magnets. At this stage, a vacuum is used to remove the air from the cap, making it rigid. Finally, the alignment fixture is removed.
2. The region around the patient's eye is sterilized.
3. Surgical draping is applied over the patient's face (Fig. 12(b)), using the same draping process used in manual surgery.

4. Trocar cannulas are inserted into the eye in the standard positions.
5. Any other preliminary surgical tasks that do not require the use of the robot are performed.
6. The mounting plate, with attached robots and counterweights, is connected to the on/off magnets through the draping (Fig. 12(c)). The robot(s) would likely be within their own sterile bags.

## 7. Evaluation of Alternative Design Concept and Comparison to Initial Design Concept

We conducted an initial study in which we used the optical motion tracker described in Sec. 5 to measure the 3D displacements of the alternative design concept to evaluate its performance. Further, we compared the displacements measured from the alternative design concept to the displacements measured in Sec. 5, which were obtained using the initial design concept.

Like the data-collection process described in Sec. 5, two of the authors were the participants. The experimental setup (Fig. 13) was the same as that used in Sec. 5, except the alternative design concept was used, and foam was placed between the plastic sheet and the design concept for comfort. The procedure followed by the participants for gentle breathing and snoring-like rapid inhalations were the same as in Sec. 5.

We represent the position of the eye relative to the tip of a robot-mounted surgical instrument as

$${}^r d_{rg} = {}^r d_{rh} + {}^o R_r^T {}^o d_{hb} + {}^o R_r^T {}^o R_b^T {}^b d_{bg}, \quad (15)$$

where  ${}^b d_{bg}$  and  ${}^r d_{rh}$  are the constant offsets calculated using (6) and (7), respectively, and  ${}^o d_{hb} = {}^o d_{ob} - {}^b d_{oh}$ . Ideally,  ${}^r d_{rg}$  would be constant if we had achieved a rigid

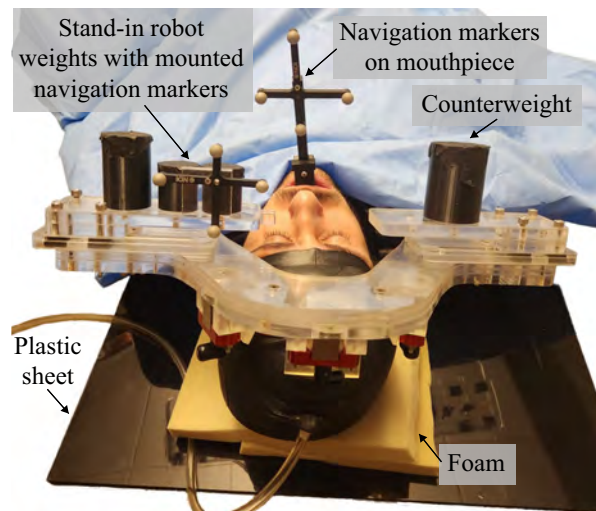


**Fig. 13.** Experimental setup used to quantify 3D relative displacements for the alternative design concept.

connection to the skull. Without loss of generality, we chose  ${}^oR_h = {}^oR_r$  (and thus  ${}^r\mathbf{d}_{rh} = {}^h\mathbf{d}_{rh}$ ) since frames  $h$  and  $r$  are rigidly connected.

Like the segmentation process for breathing data with the initial design concept in Sec. 5, we took the Fourier transform of the z-component of  ${}^o\mathbf{d}_{ob}$  for the gentle breathing results. The participants breathed with frequencies of 0.114 Hz and 0.314 Hz, respectively, which correspond to periods of 8.9 s and 3.2 s, respectively. The gentle-breathing sets were then segmented into 6 8.9 s segments and

18 3.2 s segments, respectively. Because the frequency of snoring was dictated by the 3-s intervals between beeps, we manually segmented each set of snoring data into 6 segments.

To quantify the relative displacement between the bite piece and the head-mounting prototype, we first calculate the mean relative position over the entire data set

$$\overline{{}^r\mathbf{d}_{rg}} = \frac{1}{N_{\text{tot}}} \sum_{\text{tot}} {}^r\mathbf{d}_{rg}(t), \quad (16)$$

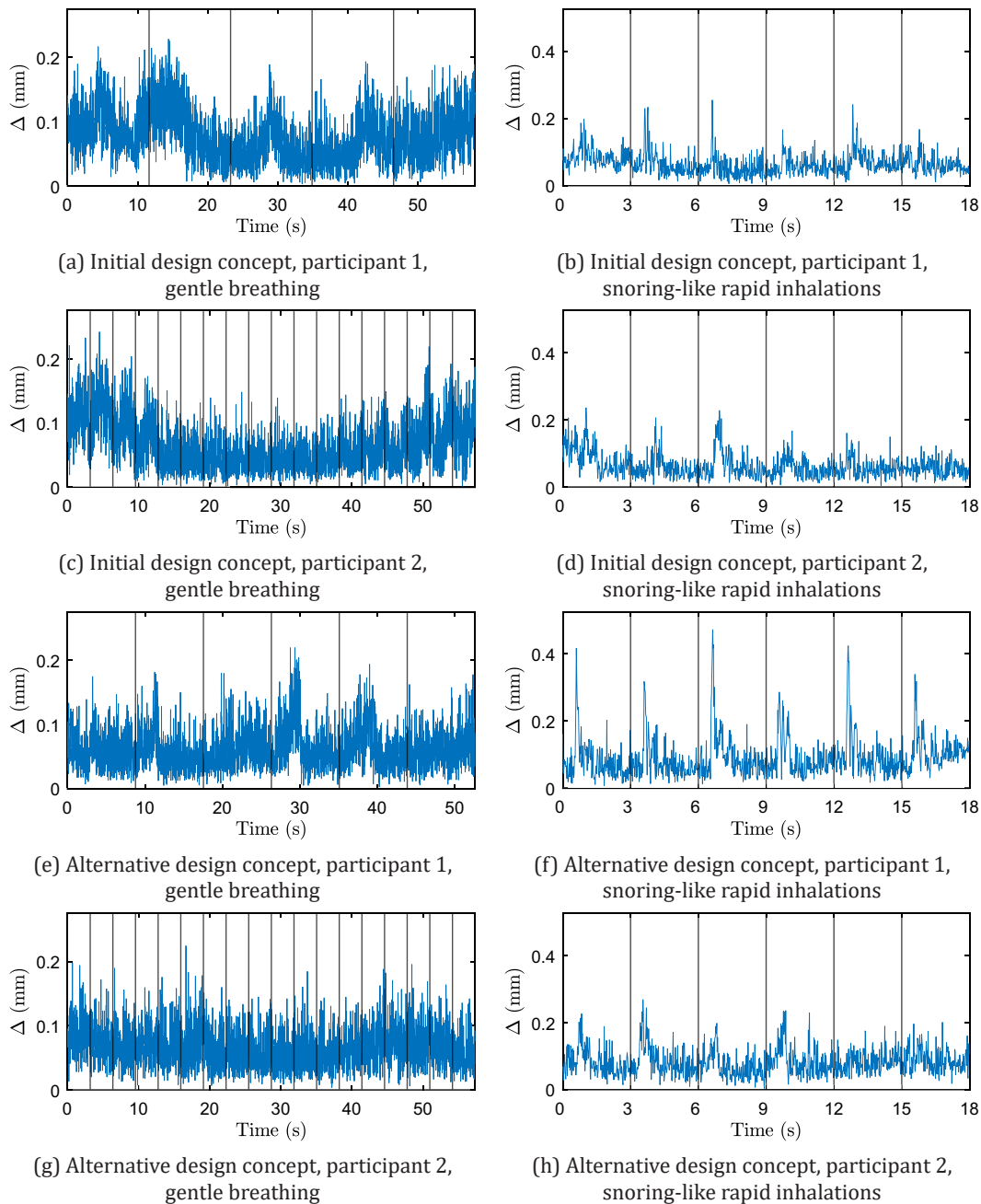


**Fig. 14.** Relative 3D displacements, calculated using (17), during gentle breathing (left column) and snoring-like rapid inhalations (right column) for Participant 1 and Participant 2. The initial design concept was used in (a)–(d), and the alternative design concept was used in (e)–(h). Vertical black lines are used to indicate where the data is segmented.

which is not (and should not be) zero. We then calculate the distance from that mean at each instant

$$\Delta(t) = \|\mathbf{r} \mathbf{d}_{rg}(t) - \overline{\mathbf{r} \mathbf{d}_{rg}}\|, \quad (17)$$

We calculate  $\Delta(t)$  for both design concepts (using the data set already gathered in Sec. 5 for the initial design concept) and segment the results into individual breathing cycles using the breathing frequencies we estimated previously. The displacements for gentle breathing with the initial design concept are shown in Figs. 14(a) and 14(c), and the displacements for the alternative design concept are shown in Figs. 14(e) and 14(g). The displacements for snoring-like rapid inhalations with the initial design concept are shown in Figs. 14(b) and 14(d), and the displacements for the alternative design concept are shown in Figs. 14(f) and 14(h).

We calculate the maximum displacement for each segment of data as

$$\Delta_{\max} = \max_{\text{seg}}(\Delta(t)). \quad (18)$$

Figure 15 shows  $\Delta_{\max}$  for both the initial and alternative design concepts. Because the displacements calculated by (17) are relative to the mean of each total data set (i.e. before segmentation), the values given by (18) capture the displacement due to each breathing cycle while also considering lower-frequency movements that occur over the course of several breathing cycles, such as the gradual displacements that are seen in the first 15 s of Fig. 14(c).

We also consider displacements that take place over shorter time scales by calculating displacements over the course of a single data segment (i.e. one breathing/snoring cycle). First, we compute the mean relative position over one breathing/snoring cycle

$$\overline{\mathbf{r} \mathbf{d}_{rg}} = \frac{1}{N_{\text{seg}}} \sum_{\text{seg}} \mathbf{r} \mathbf{d}_{rg}(t), \quad (19)$$

which is not (and should not be) zero. We then calculate the distance from that mean at each instant with that data segment

$$\delta(t) = \|\mathbf{r} \mathbf{d}_{rg}(t) - \overline{\mathbf{r} \mathbf{d}_{rg}}\|. \quad (20)$$

Finally, we calculate the maximum displacement over the course of a single data segment as

$$\delta_{\max} = \max_{\text{seg}}(\delta(t)), \quad (21)$$

which are shown in Fig. 15 for both the initial and alternative design concepts. These initial results suggest that

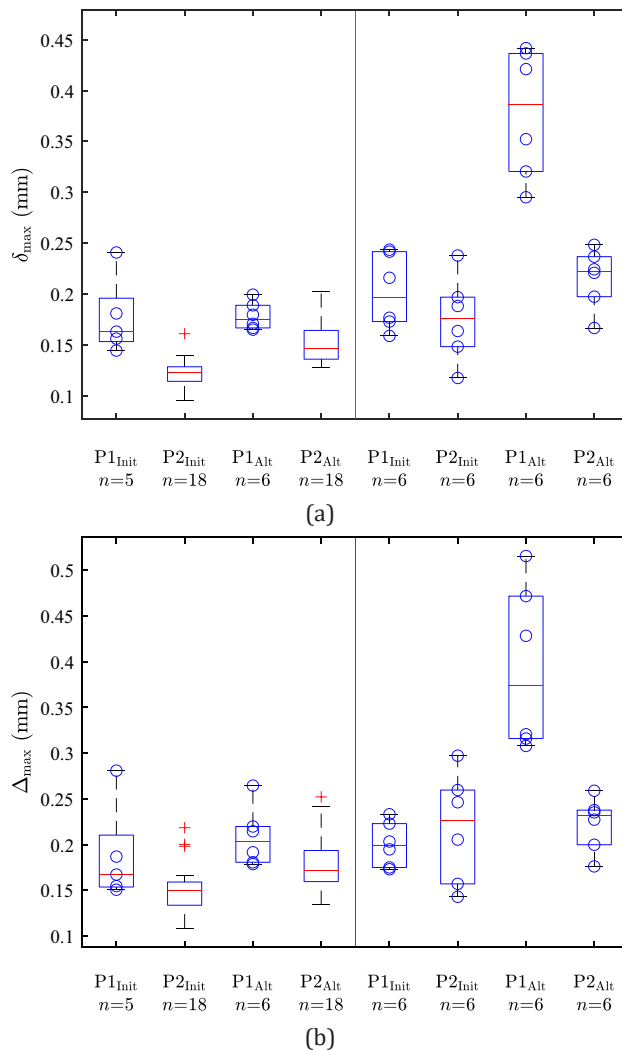


**Fig. 15.** Box-whisker plots of relative 3D motion, measured as the maximum displacements (a)  $\delta_{\max}$  and (b)  $\Delta_{\max}$  of participants P1 and P2 for gentle breathing (left) and snoring-like rapid inhalations (right) for our initial design concept (denoted by “Init”) and our alternative design concept (denoted by “Alt”). The  $n$  for each data set is provided. Raw data (blue circles) is provided when  $n < 10$ .

our alternative design concept performs comparably to our initial design concept and warrants further study.

## 8. Discussion

Mounting a robot to a patient’s head provides an approximately order-of-magnitude reduction in within-breathing-cycle movement of the robot relative to the eye orbit compared to what would be expected with a stretcher/table-mounted robot, even if the patient’s head is strapped down. Furthermore, the maximum relative displacements measured in our experiments are substantially lower than those resulting from a head-immobilization device designed to compensate for patient motion [26].



Our paradigm eliminates concern over the type of gross head drift described in [9].

The human-subjects study gives us an estimate for the displacements that can be expected from the patient population. The displacements measured over the course of several breathing cycles,  $\Delta_{\max}$ , show us that in some cases the head mount shifts on the wearer's head and does not return to its original position. Similar infrequent shifts between the head and a custom-fit thermoplastic mask have been described in studies on patient positioning accuracy for radiotherapy [38], although our experimental setup differs in that the heads of our participants were not immobilized. Participants P4 and P8 are notably different from the others in that one has markedly long and thick hair (P4) and one has a smooth bald head (P8); it is possible that hair at either extreme leads to a reduced performance with head mounting, but further studies would be required to test such a hypothesis. In the case of participant P4, the shift occurred when recording was paused (between her 19th and 20th gentle-breathing videos), and we believe the participant re-adjusted her body. It is possible that when she wore the prototype for the experiment, her head and hair (which she wore in braids) were in slightly different positions relative to the custom-fit mask and pillow than when they were formed, and her head and hair shifted to settle into the positions they were in during the originally fitting. In hindsight, allowing her to wear braids was probably ill-advised. In the case of participant P8, there was a more gradual shift that occurred across his first through seventh gentle-breathing videos.

Retinal motion that is not due to head motion (e.g. due to the patient's pulse) will not be compensated by head mounting. Such retinal motion will be present for any robotic system, and thus will not change our conclusions regarding the relative benefits of head mounting.

A practical consideration with our initial design concept is that it requires a setup period, prior to use, in order to fit the custom CIVCO cushion and thermoplastic mask to the patient. Also, the face mask may bother certain patients (e.g. with claustrophobia), although we found both the forming and donning of the face mask and custom-formed cushion to be quite comfortable. We found the alternative design concept to be comparably comfortable, but with some hair pulling during donning (as with any swim cap). Both design concepts became less comfortable after wearing them for a long duration. In our human-subjects study, any initial complaint related to comfort was due to a conflict between the goggle strap and the custom-formed components, which is an artifact of our experiment. A practical consideration with the alternative design concept is that it requires the use of a vacuum pump, which requires either introducing a pump into the operating room, or connecting a hose from the granular-jamming cap to an existing vacuum connection in the wall of the operating room. However, this design provides much better access to the rest of the face than our initial






design concept, which is particularly important for use in surgeries beyond eye surgery. Finally, we note that hearing is not appreciably impaired with either design.

In our experiments, when we looked at relative motion between our prototypes and the head, there was no tool-tissue interaction force at the robot end-effector. In eye surgery, we expect those forces to be negligible during delicate procedures of the retina, so we can reasonably expect that the benefits of head mounting as reported in this paper will apply directly to head-mounted retinal-surgery robots. However, for other types of surgeries where a robot exerts substantial forces on the head (e.g. drilling bone), one should not assume the same quantitative benefits as those reported in this paper.

## Acknowledgements

We would like to thank CIVCO for providing the Solstat Immobilization System, Dr. Ruisi Zhang for her technical assistance, and Lillian Pontacolone, Ethan Peterson, and Lori McCoy for their assistance with the experiments conducted at the Moran Eye Center. Research reported in this publication was supported by the National Eye Institute of the National Institutes of Health under Award Number R21EY027528. The content is solely the responsibility of the authors and does not necessarily represent the official views of the National Institutes of Health.

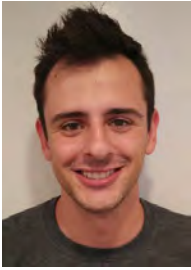
## ORCID

Nicholas R. Posselli   
<https://orcid.org/0000-0003-1563-7082>  
 Patrick S. Wellborn   
<https://orcid.org/0000-0003-0357-2998>  
 Paul S. Bernstein   
<https://orcid.org/0000-0002-4228-7666>  
 Robert J. Webster III   
<https://orcid.org/0000-0003-1389-224X>  
 Jake J. Abbott   
<https://orcid.org/0000-0002-0665-1934>

## References

1. B. A. Scruggs, H. M. Vasconcelos Jr, M. Matioli da Palma, K. Kogachi, M. E. Pennesi, P. Yang, S. T. Bailey and A. K. Lauer, Injection pressure levels for creating blebs during subretinal gene therapy, *Gene Ther.* **29**(10-11) (2022) 601–607.
2. C. E. Myers, B. E. Klein, S. M. Meuer, M. K. Swift, C. S. Chandler, Y. Huang, S. Gangaputra, J. W. Pak, R. P. Danis and R. Klein, Retinal thickness measured by spectral-domain optical coherence tomography in eyes without retinal abnormalities: The beaver dam eye study, *Am. J. Ophthalmol.* **159**(3) (2015) 445–456.
3. W. Halfter, J. Sebag and E. T. Cunningham, Vitreoretinal interface and inner limiting membrane, in *Vitreous*, ed. J. Sebag (Springer, 2014), pp. 165–191.

4. D. An, C. Balaratnasingam, M. Heisler, A. Francke, M. Ju, I. L. McAllister, M. Sarunic and D.-Y. Yu, Quantitative comparisons between optical coherence tomography angiography and matched histology in the human eye, *Exp. Eye Res.* **170** (2018) 13–19.
5. J. R. Wilkins, C. A. Puliafito, M. R. Hee, J. S. Duker, E. Reichel, J. G. Coker, J. S. Schuman, E. A. Swanson and J. G. Fujimoto, Characterization of epiretinal membranes using optical coherence tomography, *Ophthalmology* **103**(12) (1996) 2142–2151.
6. S. P. N. Singh and C. N. Riviere, Physiological tremor amplitude during retinal microsurgery, in *Proc. IEEE 28th Annual Northeast Bioengineering Conf.* (IEEE, 2002), pp. 171–172.
7. F. Peral-Gutierrez, A. L. Liao and C. N. Riviere, Static and dynamic accuracy of vitreoretinal surgeons, in *Proc. 26th Annual Int. Conf. IEEE Eng. Med. Biol. Soc. Engineering in Medicine and Biology Society* (IEEE, 2004), pp. 2734–2737.
8. J. Salmon, B. Mets, M. James and A. Murray, Intravenous sedation for ocular surgery under local anaesthesia., *Br. J. Ophthalmol.* **76**(10) (1992) 598–601.
9. K. Brogan, B. Dawar, D. Lockington and K. Ramaesh, Intraoperative head drift and eye movement: Two under addressed challenges during cataract surgery, *Eye* **32**(6) (2018) 1111–1116.
10. P.-R. Rothschild, S. Grabar, B. Le Dû, C. Temstet, O. Rostaqui and A. P. Brézin, Patients' subjective assessment of the duration of cataract surgery: A case series, *BMJ Open* **3**(5) (2013) e002497.
11. B. Loriga, A. Di Filippo, L. Tofani, P. Signorini, T. Caporossi, F. Barca, A. R. De Gaudio, S. Rizzo and C. Adembri, Postoperative pain after vitreo-retinal surgery is influenced by surgery duration and anesthesia conduction., *Minerva Anestesiol.* **85**(7) (2018) 731–737.
12. C. A. McCannel, E. J. Olson, M. J. Donaldson, S. J. Bakri, J. S. Pulido and M. Donna, Snoring is associated with unexpected patient head movement during monitored anesthesia care vitreoretinal surgery, *Retina* **32**(7) (2012) 1324–1327.
13. E. Vander Poorten, C. N. Riviere, J. J. Abbott, C. Bergeles, M. A. Nasser, J. U. Kang, R. Sznitman, K. Faridpooya and I. Iordachita, Robotic retinal surgery, in *Handbook of Robotic and Image-Guided Surgery*, ed. M. H. Abedin-Nasab (Elsevier, 2019), pp. 627–672.
14. I. I. Iordachita, M. D. De Smet, G. Naus, M. Mitsuishi and C. N. Riviere, Robotic assistance for intraocular microsurgery: Challenges and perspectives, *Proc. IEEE* **110**(7) (2022) 893–908.
15. J. Cehajic-Kapetanovic, K. Xue, T. L. Edwards, T. C. Meenink, M. J. Beelen, G. J. Naus, M. D. de Smet and R. E. MacLaren, First-in-human robot-assisted subretinal drug delivery under local anesthesia, *Am. J. Ophthalmol.* **237** (2022) 104–113.
16. A. Ebrahimi, M. G. Urias, N. Patel, R. H. Taylor, P. Gehlbach and I. Iordachita, Adaptive control improves sclera force safety in robot-assisted eye surgery: A clinical study, *IEEE Trans. Biomed. Eng.* **68**(11) (2021) 3356–3365.
17. H. Natalius, P. Lambert, M. K. Tiwari, L. da Cruz and C. Bergeles, Design, static and performance analysis of a parallel robot for head stabilisation in vitreoretinal surgery, in *New Trends in Medical and Service Robotics. MESROB 2020. Mechanisms and Machine Science*, eds. G. Rauter, P. C. Cattin, A. Zam, R. Riener, G. Carbone and D. Pisla, Vol. 93 (Springer, Cham, 2021), pp. 169–179.
18. T. L. Edwards, K. Xue, H. C. M. Meenink, M. J. Beelen, G. J. L. Naus, M. P. Simunovic, M. Latasiewicz, A. D. Farmery, M. D. de Smet and R. E. MacLaren, First-in-human study of the safety and viability of intraocular robotic surgery, *Nat. Biomed. Eng.* **2** (2018) 649–656.
19. K. Faridpooya, S. H. van Romunde, S. S. Manning, J. C. van Meurs, G. J. Naus, M. J. Beelen, T. C. Meenink, J. Smit and M. D. de Smet, Randomized controlled trial on robot-assisted vs manual surgery for pucker peeling, *Clin. Exp. Ophthalmol.* **50**(9) (2022) 1057–1064.
20. K. Willekens, A. Gijbels, J. Smits, L. Schoevaerdt, J. Blanckaert, J. H. Feyen, D. Reynaerts and P. Stalmans, Phase I trial on robot assisted retinal vein cannulation with ocriplasmin infusion for central retinal vein occlusion, *Acta Ophthalmol.* **99**(1) (2021) 90–96.
21. X. He, J. Handa, P. Gehlbach, R. Taylor and I. Iordachita, A submillimetric 3-DOF force sensing instrument with integrated fiber Bragg grating for retinal microsurgery, *IEEE Trans. Biomed. Eng.* **61**(2) (2014) 522–534.
22. B. C. Becker, R. A. MacLachlan, L. A. Lobes, G. D. Hager and C. N. Riviere, Vision-based control of a handheld surgical micromanipulator with virtual fixtures, *IEEE Trans. Robot.* **29**(3) (2013) 674–683.
23. Y. Han, A. Routray, J. O. Adeghate, R. A. MacLachlan, J. N. Martel and C. N. Riviere, Monocular vision-based retinal membrane peeling with a handheld robot, *J. Med. Devices* **15**(3) (2021).
24. M. A. Nasser, M. Eder, S. Nair, E. C. Dean, M. Maier, D. Zapp, C. P. Lohmann and A. Knoll, The introduction of a new robot for assistance in ophthalmic surgery, in *Proc. 35th Annual Int. Conf. IEEE Engineering in Medicine and Biology Society* (IEEE, 2013), pp. 5682–5685.
25. K. Huang, M. Zhou, C. Lajblich, C. P. Lohmann, A. Knoll, Y. Ling, H. Lin and M. A. Nasser, A flexible head fixation for ophthalmic microsurgery, in *Chin. Autom. Congr.* (IEEE, 2017), pp. 6707–6710.
26. M. A. Nasser, M. Maier and C. P. Lohmann, A targeted drug delivery platform for assisting retinal surgeons for treating age-related macular degeneration (AMD), in *Proc. 39th Annual Int. Conf. IEEE Engineering in Medicine and Biology Society* (IEEE, 2017), pp. 4333–4338.
27. S. Guo, N. R. Sarfaraz, W. G. Gensheimer, A. Krieger and J. U. Kang, Demonstration of optical coherence tomography guided big bubble technique for deep anterior lamellar keratoplasty (DALK), *Sensors* **20**(2) (2020) 428.
28. M. Nambi, P. S. Bernstein and J. J. Abbott, A compact telemanipulated retinal-surgery system that uses commercially available instruments with a quickchange adapter, *J. Med. Robot. Res.* **1**(2) (2016) 1630001.
29. W. Wei, R. Goldman, N. Simaan, H. Fine and S. Chang, Design and theoretical evaluation of microsurgical manipulators for orbital manipulation and intraocular dexterity, in *Proc. IEEE Int. Conf. Robotics and Automation* (IEEE, 2007), pp. 3389–3395.
30. N. R. Posselli, P. S. Bernstein and J. J. Abbott, Headmounting surgical robots for passive motion compensation, in *Proc. Hamlyn Symp. Medical Robotics* (Imperial College London, 2022), pp. 95–96.
31. P. S. Wellborn, N. P. Dillon, P. T. Russell and R. J. Webster III, Coffee: The key to safer image-guided surgery—a granular jamming cap for non-invasive, rigid fixation of fiducial markers to the patient, *Int. J. Comput. Assist. Radiol. Surg.* **12**(6) (2017) 1069–1077.
32. J. S. Schneider, J. Burgner, R. J. Webster III and P. T. Russell III, Robotic surgery for the sinuses and skull base: What are the possibilities and what are the obstacles? *Curr. Opin. Otolaryngol. Head Neck Surg.* **21**(1) (2013) 11–16.
33. V. Trévilot, R. Garrel, E. Dombre, P. Poignet, R. Sobral and L. Cramette, Robotic endoscopic sinus and skull base surgery: Review of the literature and future prospects, *Eur. Ann. Otorhinolaryngol. Head Neck Dis.* **130**(4) (2013) 201–207.
34. R. F. Labadie, J. H. Noble, B. M. Dawant, R. Balachandran, O. Majdani and J. M. Fitzpatrick, Clinical validation of percutaneous cochlear implant surgery: Initial report, *Laryngoscope* **118**(6) (2008) 1031–1039.
35. K. E. Riojas and R. F. Labadie, Robotic ear surgery, *Otolaryngol. Clin. North Am.* **53**(6) (2020) 1065–1075.
36. J. Granna, E. B. Pitt, M. E. McKay, T. J. Ball, J. S. Neimat, D. J. Englot, R. P. Naftel, E. J. Barth and R. J. Webster III, Targeting epilepsy through the foremen ovale: How many helical needles are needed? *Ann. Biomed. Eng.* **50**(5) (2022) 499–506.
37. P. S. Wellborn, P. T. Russell and R. J. Webster III, A multi-subject accuracy study on granular jamming for non-invasive attachment of fiducial markers to patients, *Int. J. Comput. Assist. Radiol. Surg.* **15**(1) (2020) 69–74.
38. T. J. Bichay and A. Mayville, The continuous assessment of cranial motion in thermoplastic masks during CyberKnife radiosurgery for trigeminal neuralgia, *Cureus* **8**(5) (2016) 1–9.



**Nicholas R. Posselli** received his B.S. degree in Mechanical Engineering from the University of Utah, USA, in 2016. He is currently pursuing the Ph.D. degree in Mechanical Engineering (Robotics Track) from the University of Utah. His research interests are in surgical robotics.



**Robert J. Webster, III** received his B.S. degree in Electrical Engineering from Clemson University, USA, in 2002, and his M.S. and Ph.D. degrees in Mechanical Engineering from Johns Hopkins University, USA, in 2004 and 2007, respectively. In 2008, he joined the faculty of the Department of Mechanical Engineering, Vanderbilt University, USA, where he is now a Professor. He directs the Medical and Electromechanical Design Laboratory. His research interests include medical robotics, image-guided surgery, and continuum robotics.



**Patrick S. Wellborn** received his B.S. degree in Chemistry Engineering from Washington and Lee University, USA, in 2015, and his Ph.D. degree in Mechanical Engineering from Vanderbilt University, USA, in 2021. He is currently an engineer with Titan Medical, USA. His research interests include surgical robotics and image-guided surgery.



**Jake J. Abbott** received his B.S. degree from Utah State University, USA, his M.S. degree from the University of Utah, USA, and his Ph.D. degree from Johns Hopkins University, USA, all in Mechanical Engineering, in 1999, 2001, and 2006, respectively. He was a Postdoctoral Researcher at ETH Zurich, Switzerland until 2008, when he joined the faculty of the Department of Mechanical Engineering, University of Utah, USA, where he is now a Professor. He directs the Magnetic and Medical Robotics Laboratory. His research interests

include medical robotics, magnetics applied to robotics, and haptics.



**Paul S. Bernstein** received his B.S. degree in Chemistry in 1981, and his Ph.D. degree in Pharmacology in 1988, from Harvard University, USA. He received his M.D. degree in 1988 from the Division of Health Sciences and Technology, a joint program between Harvard Medical School and the Massachusetts Institute of Technology, USA. He did a postdoctoral fellowship in Cell Biology and a residency in Ophthalmology at the Jules Stein Eye Institute, University of California, Los Angeles, USA. In 1995, he joined the faculty of the Moran Eye

Center of the University of Utah, USA, where he is now a Professor of Ophthalmology and Visual Sciences. He divides his time equally between basic-science retina research and a clinical practice devoted to medical and surgical treatment of disease of the retina and vitreous.